BACKSCATTER-BASED UAV-ENABLED MOBILE EDGE COMPUTING IoT NETWORK: DESIGN AND ANALYSIS

Dac-Binh Ha[1], Van-Truong Truong[1]*, Tien-Vu Truong[1], Nguyen-Son Vo[2], Van Nhan Vo[1]

[1]Duy Tan University, Da Nang, Vietnam

[2]Institute of Fundamental and Applied Sciences, Duy Tan University, Ho Chi Minh City, Vietnam

*Corresponding author: truongvantruong@dtu.edu.vn

(Received: June 24, 2024; Revised: October 19, 2024; Accepted: October 24, 2024)

DOI: 10.31130/ud-jst.2024.321E

Abstract - In the 6G mobile networks, ensuring low latency and low energy consumption is paramount. This study explores a novel approach for addressing these issues in a backscatter communication (BC) - based multiple user unmanned aerial vehicle (UAV) - enabled mobile edge computing (MEC) Internet of Things (IoT) network. Our proposed framework incorporates a partial offloading strategy, a time division multiple access (TDMA) scheme, and a radio frequency energy harvesting mechanism. We use the channel gains statistical characteristics to derive approximate closed-form expressions for the successful computation and energy outage probabilities. Using these benchmarks, we investigate the impact of critical parameters such as transmit power, number of sensor nodes, task division ratio, the altitude of the UAV, and threshold tolerance. We validate our analysis through computer simulations and provide results to support our findings. The study reveals that selecting an optimal UAV altitude can significantly improve latency and energy consumption performance.

Key words - Mobile edge computing; partial offloading; unmanned aerial vehicle; backscatter; RF energy harvesting.

1. Introduction

Mobile edge computing (MEC) is crucial in unlocking the potential of 6G networks, supporting various innovative applications and services that require ultra-low latency, high reliability, and intelligent edge processing capabilities [1], [2]. MEC brings computation and storage closer to the edge of the network, reducing the latency experienced by mobile users. In 6G networks, this could enable real-time applications like autonomous vehicles, augmented reality (AR), and virtual reality (VR) to operate seamlessly. By offloading processing tasks to edge servers, MEC can alleviate congestion on the core network, leading to more efficient bandwidth utilization. It is crucial as 6G networks aim to support massive connectivity and higher data rates. MEC can also improve network reliability by distributing processing tasks across multiple edge servers, reducing the impact of individual server failures. This resilience is essential for critical healthcare, transportation, and industrial automation applications. With MEC, artificial intelligence (AI) and machine learning (ML) models can be deployed directly at the network edge, enabling real-time intelligent decision-making without relying exclusively on centralized cloud infrastructure. It facilitates various use cases, including context-aware services and predictive maintenance. MEC enables network slicing, allowing operators to create virtualized, customized network instances tailored to specific application requirements. In 6G networks, this capability can support diverse use cases with varying performance, security, and resource requirements. MEC enables data processing and analytics to be performed closer to the data source, reducing the need to transmit sensitive information over long distances. It enhances privacy and compliance with data localization regulations, which are becoming increasingly stringent globally.

In recent years, we have also seen MEC networks being applied more in the IoT field, combining BC technology [3]. BC is a method to transmit data by reflecting signals to a receiver rather than generating its signals [4]. It is commonly used in radio frequency identification (RFID) systems and wireless communication devices. In backscatter technology, a device modulates and reflects an incoming signal to convey information, enabling communication without requiring its power source for signal transmission. Accordingly, BC is suitable for low-power communication applications, such as IoT devices and wireless sensors [5]. It can lead to significant energy savings, extended battery life, and increased deployment possibilities for applications in 6G networks [2], [6].

Meanwhile, UAVs can be utilized for various purposes, such as aerial base stations, edge computing, network coverage expansion, traffic monitoring, and disaster management [7]. Their ability to quickly deploy and navigate rugged terrain makes them valuable assets for improving connectivity and computing assistance, especially in remote or inaccessible areas. Additionally, UAVs can support dynamic network optimization and resource management, contributing to the efficiency and reliability of 6G networks [2], [8]. In order to prolong the lifetime of connectivity, RF (Radio Frequency) energy harvesting holds significant potential in 6G networks [9]. With the expected proliferation of small cell deployments, massive MIMO systems, and mmWave technologies in 6G, abundant ambient RF energy will be available for harvesting. This energy can power low-power devices, sensors, and IoT devices, extending their battery life or enabling battery-free operation. Additionally, RF energy harvesting can contribute to sustainability efforts by reducing the need for conventional power sources in wireless communication networks. However, challenges such as efficient energy conversion, RF signal variability, and interference mitigation must be addressed to fully leverage the potential of RF energy harvesting in 6G networks.

This paper explores how backscatter, UAV and RF energy harvesting, and MEC technologies can be integrated into IoT networks. The main contributions of the paper are summarized as follows:

- We introduce an innovative framework for a UAV-enabled MEC IoT system utilizing backscatter technology, featuring a partial offloading strategy, time division multiple access scheme, and RF energy harvesting mechanism.
- We derive approximate closed-form expressions for the successful computation probability (SCP) and energy outage probability (EOP) using the statistical characteristics of channel gains.
- We examine how key parameters like transmit power, task division ratio, UAV altitude, number of sensor nodes, and threshold latency affect the system. Furthermore, we offer computer simulation results to validate our analysis.

2. Related works

Numerous studies have explored the integration of backscatter, UAV and RF energy harvesting, and MEC technologies in IoT networks [10]-[18]. In their paper [13], the authors introduced a combined architecture integrating backscattering and uplink nonorthogonal multiple access (NOMA) for MEC IoT networks. They performed joint resource allocation, considering the communication capability of each IoT node and the computational resources of both the nodes and the MEC server. The study described in [14] explores the combination of backscattering, RF energy harvesting, and intelligent reconfigurable surfaces in the MEC network, employing the time-division multiple access (TDMA) scheme. The work [15] focused on the computing task offloading and resource allocation scheme in UAV-aided backscatter MEC networks. The UAV is the RF station, while the ground station is the access point. The problem of minimizing the total energy consumption of UAVs is formulated and solved by the successive convex approximation method. The study [16] explored how energy efficiency can be improved in an MEC network with UAV assistance. The UAV is a mobile energy source and edge computing platform, offering ground-based users battery charging and computational services. However, this work did not utilize the backscattering technology. The study [17] investigated a multi-antenna UAV-assisted communication system for transmitting short packets using backscatter technology. The optimization problems aimed at maximizing throughput while considering the number of transmit bits and the UAV altitude and minimizing block error rate were formulated and solved using the one-dimensional search method. Similarly, the work [18] investigated a system's performance in which UAV assisted multiple backscattering devices in wireless energy charging and data transmission. Using a search algorithm, they formulated and solved an optimization problem to maximize energy efficiency and minimize transmit power. However, the MEC system was not taken into account in these two works [17], [18].

The studies mentioned in the literature have not overlooked the potential advantages of incorporating backscatter, RF energy harvesting, and UAV-enabled techniques into MEC networks. Our study proposes a UAV-enabled MEC IoT network utilizing backscatter technology. This network features a partial offloading strategy, a time division multiple access scheme, and an RF energy harvesting mechanism. In this setup, the UAV functions as a mobile edge server, offering computational resources for ground users. The ground station, on the other hand, provides an unmodulated signal that facilitates task offloading from the users to the UAV.

3. System and Channel Model Description

3.1. System and Channel Models

Figure 1 illustrates a backscatter-based multiple smart sensor node and unmanned aerial vehicle-enabled MEC in the IoT system. It comprises one ground-dedicated RF station (denoted as **S**), one single-antenna UAV access point (denoted as **U**), and K resource-constrained single-antenna ground smart nodes (denoted as **SN**s). The **U** is integrated with an edge server and hovers in the sky at an altitude z_U to assist smart nodes in executing their tasks. The station **S** provides RF signals to **SN**s for employing BC. Assuming that **U** and **SN**s operate in haft-duplex mode. The static Cartesian coordinate is used to present the location of the UAV and each node. Thus, we denote the location of **U** as (x_U, y_U, z_U), the location of k^{th} $\mathbf{SN}_k$ as (x_k, y_k, 0) with $k \in \{1,...,K\}$, and the location of **S** as (x_S, y_S, 0).

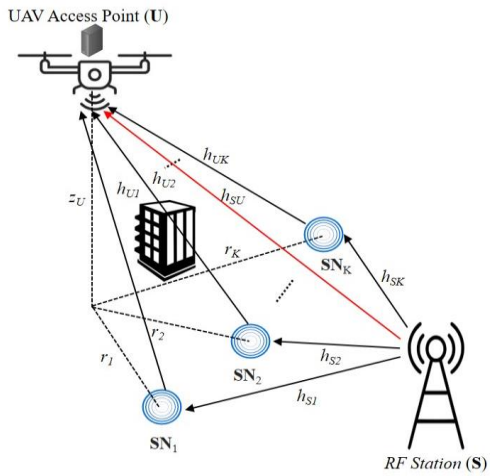

Figure 1. *System model for BC-based multi-user UAV-MEC IoT Network*

We can model the signal fading in ground-to-air (G2A) and air-to-ground (A2G) communication channels using large-scale and small-scale fading. Large-scale fading depends on the probability of a direct line-of-sight (LoS) or indirect non-line-of-sight (NLoS) path, as described in [19]. Small-scale fading refers to rapid signal fluctuations due to local effects, and we can represent it using the Nakagami-m distribution with parameter m [20]. Now, considering the probability of both LoS and NLoS links between the **U** and the k^{th} $\mathbf{SN}_k$, we can express the average path loss as:

$$\mathcal{L}_{Uk}\left(d_{Uk},\theta_{Uk}\right)=\left[\mathcal{J}_{\mathrm{LoS}}+\frac{\mathcal{J}_{\mathrm{LoS}}-\mathcal{J}_{\mathrm{NLoS}}}{1+be^{\left(-\frac{180}{\pi}a\theta_{Uk}+ab\right)}}\right]d_{Uk}^{\alpha}, \quad (1)$$

where $d_{Uk}=\sqrt{\left(x_U-x_k\right)^2+\left(y_U-y_k\right)^2+z_U{}^2}$,

$\theta_{Uk} = \arcsin\left(z_U / d_{Uk}\right)$, α stands for the path-loss exponent, a and b represent parameters whose values change based on the surrounding environment, and $\mathcal{J}_A = \Psi_V \left(c / 4\pi f_c\right)^{-1}$, $A \in \{\text{LoS}, \text{NLoS}\}$, denotes the parameter depended on environment and carrier frequency f_c, c denotes the speed of light, and Ψ_V represents the excessive path loss of the LoS and NLoS propagation [21].

The channel coefficients of **U**-**SN**$_k$, **S**-**SN**$_k$ and **S**-**U** links are denoted as h_{Uk}, h_{Sk} and h_{SU}, respectively. The cumulative distribution function (CDF) and the probability density function (PDF) of corresponding power channel gains, $|h_{Uk}|^2$, $|h_{Sk}|^2$ and $|h_{SU}|^2$, are, respectively, as follows:

$$F_X(x) = 1 - e^{-\frac{m_X}{\lambda_X}x} \sum_{l=0}^{m_X-1} \frac{1}{l!}\left(\frac{m_X}{\lambda_X}x\right)^l, \quad (2)$$

$$f_X(x) = \frac{1}{(m_X-1)!}\left(\frac{m_X}{\lambda_X}\right)^{m_X} x^{m_X-1} e^{-\frac{m_X}{\lambda_X}x}, \quad (3)$$

where $X \in \{|h_{Uk}|^2, h_{Sk}|^2, |h_{SU}|^2\}$, $\lambda_X = \mathbf{E}[X]$, $\mathbf{E}[.]$ stands for expectation operator, $m_X \geq 0.5$ is the fading severity factor. For simplicity, $m_{|h_{Sk}|^2} = m_1, m_{|h_{Uk}|^2} = m_2$, $\lambda_{|h_{Sk}|^2} = \lambda_1$, $\lambda_{|h_{Uk}|^2} = \lambda_2$, $\forall k \in \{1,...,K\}$, $g_{Uk} = |h_{Uk}|^2, g_{Sk} = |h_{Sk}|^2$ and $g_{SU} = |h_{SU}|^2$.

3.2. Signal Models

In this study, a TDMA strategy is considered as Figure 2. For simplicity, the entire operation duration *T* is divided into *N* equal time slots; thus, the time duration of each slot is $\delta = T/N$. The n^{th} ($\forall n \in \{1,...,N\}$) time slot with the length of δ is divided again into *K* small time slots which is denoted as $\tau_k[n]$, $\forall k \in \{1,...,K\}$. The length of each slot depends on the offloading time for each **SN**.

Due to BC, the transmitted carrier signal, represented as *s*[*n*], from the dedicated **S**, can cause an interference to the received backscattered signal at **U**. This interference can be eliminated by implementing perfect successive interference cancellation (pSIC) at **U**. Therefore, the signal received at **U** can be given by

$$y_k[n] = \sqrt{\frac{\xi_k P_s}{\mathcal{L}_{Uk} d_{Sk}^{\alpha}}} s[n]\varepsilon[n] h_{Sk}[n] h_{Uk}[n] + w[n], \quad (4)$$

Where, P_s is the transmit power of **S**, ξ ($0 < \xi < 1$) denotes the backscattering reflection coefficient **SN**s, $\varepsilon_k[n] \in \{0,1\}$ $\mathbf{E}[s[n]^2] = \mathbf{E}[\varepsilon_k[n]^2] = 1$, $\mathbf{E}[.]$ stands for the expectation operator, d_{Sk} represents the Euclidean distances from the k^{th} **SN** to **S**, and *w*[*n*] denotes the additive white Gaussian noise (AWGN), which has zero mean and variance of σ^2. The instantaneous signal-to-noise ratio (SNR) received at **U** is obtained as

$$\gamma_k = \frac{\xi \gamma_s |h_{Sk}|^2 |h_{Uk}|^2}{\mathcal{L}_{Uk} d_{Sk}^{\alpha}} = \mu g_{Sk} g_{Uk}, \quad (5)$$

where $\gamma_s = P_s / \sigma^2$, $\mu = \xi \gamma_s / \left(\mathcal{L}_{Uk} d_{Sk}^{\alpha}\right)$.

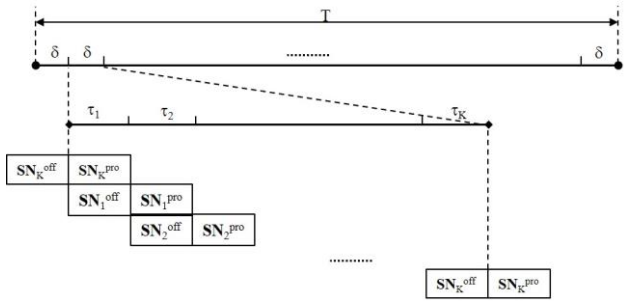

Figure 2. *Time diagram of work flow for our proposed system*

3.3. Offloading and Edge Computing Models

In our work, a partial offloading scheme is considered. In this scheme, the smart user nodes with limited energy and computation resources can handle their partial tasks locally and offload the remainders to **U** for processing through deployed BC. We assume that the server at **U** processes the tasks in a pipeline manner. Each **SN**'s task can be divided into two independent $L_{k1} = \rho_k L_k$ - bit and $L_{k2} = (1-\rho_k) L_k$ -bit subtasks, where $0 \leq \rho_k \leq 1$ is the task dividing ratio and L_k represents the total bit length of the k^{th} **SN**'s task. According to Figure 2, the workflow of this proposed system is described as follows:

- During the duration $\tau_k[n]$, the k^{th} **SN** computes its L_{k1} -bit subtask locally and offloads its L_{k2} -bit remainder to **U**. Throughout the remaining time, it harvests energy from **S** by employing an RF power harvesting scheme. The corresponding executing time at the k^{th} **SN** can be expressed as

$$t_k^c = \frac{c_k L_{k1}}{f_k} = \frac{c_k \rho_k L_k}{f_k}, \quad (6)$$

where c_k and f_k denote the CPU cycles for node *k* to compute one bit and its CPU-cycle frequency. The time consumption for offloading is calculated as

$$t_k^{\text{off}} = \frac{L_{k2}}{W \log_2\left(1+\gamma_k\right)}, \quad (7)$$

where *W* denotes the channel bandwidth for each user *k*.

- The **U** receives the offloading data from the k^{th} **SN**, denoted as $\mathbf{SN}_k^{\text{off}}$, and processes the previous received data from the $(k-1)^{th}$ **SN**, denoted as $\mathbf{SN}_{k-1}^{\text{pro}}$, simultaneously. In other words, the offloading and computing routines for each user are executed at **U** in two continuous time slots (τ_k and τ_{k+1}). The corresponding executing time at the **U** is obtained as

$$t_k^U = \frac{c_U L_{k2}}{f_U} = \frac{c_U (1-\rho_k) L_k}{f_U}, \quad (8)$$

where c_U and f_U denote the CPU cycles per bit computing and the CPU-cycle frequency of **U**'s server.

Note: Assuming that the position of **U** remains nearly unchanged during each time slot δ and across different time slots, it can be moved. Accordingly, the position of **U** at n^{th} time slot is ($x_U[n]$, $y_U[n]$, $z_U[n]$), $\forall n \in \{1,...,N\}$. We further assume that the time of result feedback to each **SN** is small compared to $\tau_k[n]$. Thus, it is neglected.

3.4. Energy Models

In our work, we propose that the smart nodes can harvests the RF energy from RF station. Thus, the harvested energy of each **SN** is obtained as

$$E_k^h = \eta P_s \frac{|h_{Sk}|^2}{d_{Sk}^{\alpha}}\left(\delta - t_k^{off} - t_k^c\right), \tag{9}$$

where $0 < \eta \le 1$ denotes the energy conversion efficiency of **SN.** Assuming that all **SN**s have the same energy conversion efficiency. The smart nodes are designed so that the harvested energy is utilized to compute the L_{k1}-bit subtask, i.e., $E_k^h > 0$. According to [22], the energy consumption of the k^{th} **SN** is calculated as

$$E_k^c = \kappa_k c_k (f_k)^2 L_{k1} = \kappa c_k (f_k)^2 \rho_k L_k, \tag{10}$$

where κ stands for the effective capacitance coefficients of CPU with relation to the CPU architecture in the k^{th} **SN**. Therefore, each task can be divided to satisfy

$$E_k^h \ge E_k^c. \tag{11}$$

In other words, we can select the value of task dividing ratio, ρ_k, according to (9).

The energy consumption of **U** consists of two parts: One is for computing (E_U^c) and other is for flying (E_U^f). The total energy consumption for executing in **U** is obtained as

$$E_U^c = \kappa_U c_U (f_U)^2 \sum_{k=1}^{K} L_{k2} = \kappa_U c_U (f_U)^2 \sum_{k=1}^{K} (1-\rho_k) L_k, \tag{12}$$

Where, κ_U stands for the effective capacitance coefficients of CPU with relation to the CPU architecture in **U**.

Consider UAV having multiple rotors, the power consumed when flying in the sky due to gravity force can given by [20]

$$P_U^f = \sqrt{\frac{(W_U g)^3}{2\varpi \kappa r}}, \tag{13}$$

where, W_U stands for the UAV's weight, g is the standard acceleration of gravity, ϖ is the fluid air density, ϑ is the rotor disc area, and n is the number of rotors.

4. Performance Analysis

4.1. Successful Computation Probability (SCP)

This subsection analyzes the performance analysis regarding SCP, denoted as $\mathcal{P}$. This criterion is the key metric to evaluate the latency performance of MEC systems [23]. SCP is the probability that the MEC latency, including offloading time and computation time, is lower than the pre-given time. Considering the condition of $E_k^h > 0$, the SCP of this considered system can be defined as follows:

$$\begin{aligned}\mathcal{P} &= \prod_{k=1}^{K} \Pr\left(t_k^{off} + \max\left(t_k^c, t_k^U\right) < T_k^{th}, E_k^h > 0\right) \\ &= \prod_{k=1}^{K} \Pr\left(t_k^{off} + t_k^c < T_k^{th}, t_k^{off} + t_k^U < T_k^{th}, E_k^h > 0\right).\end{aligned} \tag{14}$$

The approximately closed-form expression of SCP is depicted as **Theorem 1**.

Theorem 1. The SCP of proposed backscatter-based multi-user UAV-enable MEC IoT system is given by:

$$\mathcal{P} = 2\prod_{k=1}^{K}\left(\sum_{l_1=0}^{m_1-1} \frac{1}{l_1!(m_2-1)!} \upsilon^{m_2+l_1} \mathcal{K}_{m_2-l_1}(2\upsilon)\right), \tag{15}$$

where $\upsilon = \sqrt{\frac{m_1 m_2 \Lambda}{\lambda_1 \lambda_2 \mu}}$, $\Lambda = \max\left(\Lambda_1, \Lambda_2, \Lambda_3\right)$, $\Lambda_1 = 2^{\frac{L_{k2}}{W(T_k^{th} - t_k^U)}} - 1$, $\Lambda_2 = 2^{\frac{L_{k2}}{W(T_k^{th} - t_k^c)}} - 1$, $\Lambda_3 = 2^{\frac{L_{k2}}{W(\delta - t_k^c)}} - 1$, $\mathcal{K}_v(.)$ is the modified Bessel function of the second kind with v^{th} order.

Proof. See Appendix A.

4.2. Energy Outage Probability (EOP)

This subsection analyzes the performance analysis regarding EOP of the considered system. The energy outage event is determined as the event where the energy consumption at each **SN** is larger than the harvested energy (E_k^h), or the power consumption at **U** is larger than the allocated energy budget accompanying each node, E_k^{th}. Therefore, we obtain the EOP defined as follows:

$$\mathcal{E} = 1 - \prod_{k=1}^{K} \Pr\left[E_k^c < E_k^h, P_U^f t_k^{\text{off}} + E_U^c < E_k^{th}\right]. \tag{16}$$

The approximately closed-form expressions of EOP is depicted as **Theorem 2**.

Theorem 2. The EOP of proposed backscatter-based multi-user UAV-enable MEC IoT system is given by:

$$\mathcal{E} = 1 - \prod_{k=1}^{K} \begin{cases} 0, & \text{if } E_U^c \ge E_k^{th} \,\|\, t_k^c \ge \delta \\ I_1 + I_2, & \text{others,} \end{cases} \tag{17}$$

where $\Psi = \frac{1}{(m_1-1)!}\left(\frac{m_1}{\lambda_1}\right)^{m_1}$, $\Omega_1 = \frac{E_k^c . d_{Sk}^{\alpha}}{\eta P_S}$, $\Omega_2 = \frac{E_k^{th} - E_U^c}{P_U^f}$, $\Delta(x) = 2^{\frac{L_{k2}}{W\left(\delta - t_k^c - \frac{\Omega_1}{x}\right)}} - 1$, $\Theta = 2^{\frac{L_{k2}}{W\Omega_2}} - 1$, $\phi_1 = \frac{\Omega_1}{\delta - t_k^c}$, $\phi_2 = \frac{\Omega_1}{\delta - t_k^c - \Omega_2}$, $\phi_3 = \frac{\Omega_1}{\delta - t_k^c - \Omega_2}$, $x_q = \cos\left(\frac{2q-1}{2Q}\pi\right)$, $t_q = \frac{x_q + 1}{2}\exp(-\phi_1)$, $l_q = \frac{x_q + 1}{2}(\phi_2 - \phi_1)$, $h_q = \frac{x_q + 1}{2}\exp(-\phi_3)$, Q is the complexity-vs-accuracy trade-off coefficient.

$$I_1 = \begin{cases} \Psi \sum_{l=0}^{m_2-1} \frac{1}{l!}\left(\frac{m_2}{\lambda_2 \mu}\right)^l \frac{\pi \exp(-\phi_1)}{2Q} \sum_{q=1}^{Q} \exp\left(\frac{m_2}{\lambda_2} . \frac{\Delta\left(-\ln(t_q)\right)}{\mu \ln(t_q)}\right) \left(-\ln(t_q)\right)^{m_1-l-1} \Delta^l\left(-\ln(t_q)\right) t_q^{\frac{m_1}{\lambda_1}-1} \sqrt{1-x_q^2}, & t_k^c + \Omega_2 \ge \delta \\ \Psi \sum_{l=0}^{m_2-1} \frac{1}{l!}\left(\frac{m_2}{\lambda_2 \mu}\right)^l \frac{\pi(\phi_2 - \phi_1)}{2Q} \sum_{q=1}^{Q} \exp\left(-\frac{m_1}{\lambda_1} l_q - \frac{m_2}{\lambda_2} . \frac{\Delta(l_q)}{\mu l_q}\right) l_q^{m_1-l-1} \Delta^l(l_q) \sqrt{1-l_q^2}, & t_k^c + \Omega_2 < \delta \end{cases}$$

$$I_2 = \begin{cases} 0, & t_k^c + \Omega_2 \geq \delta \\ \Psi \sum_{l=0}^{m_2-1} \frac{1}{l!} \left(\frac{m_2 \Theta}{\lambda_2 \mu} \right)^l \frac{\pi \exp(-\phi_3)}{2Q} \sum_{q=1}^{Q} \frac{\left(-\ln(h_q)\right)^{m_1-l-1} h_q^{\frac{m_1}{\lambda_1}-1}}{\exp\left(\frac{m_2 \Theta}{\lambda_2 \mu} \frac{1}{\ln(h_q)} \right)} \sqrt{1-x_q^2}, & t_k^c + \Omega_2 < \delta \end{cases}$$

Proof. See Appendix B.

5. Numerical Results and Discussion

This section assessed the backscatter-based UAV-enabled MEC IoT network's performance through SCP and EOP using Monte Carlo simulations. Table 1 summarizes the simulation parameters used [20].

Table 1. *Typical values of simulation parameters*

Parameters	Notation	Typical values
The average transmit SNR	γ_S	0 - 20 dB
The number of **SN**	K	2, 5, 10
The Nakagami-*m* severity factor	m_1, m_2	1, 2, 3
The energy conversion efficiency	η	0.1, 0.5, 0.9
The backscattering reflection coefficient	ξ	0-1
The data dividing ratio	ρ_k	0-1
The carrier frequency	f_c	2 GHz
The excessive path loss coefficients	Ψ_{LoS}, Ψ_{NLoS}	1, 20
The environment-based parameters	a, b	9.6177, 0.1581
The MEC servers CPU frequency at U	f_U	2 GHz
The **SN** CPU frequency	f_k	1 GHz
The number of CPU cycle to compute 1 bit	c_k, c_U	2
The effective CPU architecture of **SN** and U	κ_k , κ_U	10^{-23}
The channel bandwidth	W	1 MHz
The threshold of **SN** latency	T_k^{th}	0.05, 0.1, 0.2 s
The stored energy budget	E_k^{th}	1 kJ
Standard acceleration of gravity	g	9.8 m/s^2
Fluid density of air	ϖ	1.225 kg/m^3
The task length	L	50 – 500 kbit
Area of rotor disk	ϑ	0.2 m^2
Number of rotors	r	6

Figure 3 depicts the impact of critical parameters, average transmit SNR (γ_S), on the system performance. Firstly, it is observed that increasing γ_S leads to an enhancement in system performance. In simpler terms, the SCP tends to improve as the transmit power increases, whereas the EOP tends to decrease. It indicates that there is no trade-off between these two performance metrics. However, it is noteworthy that as γ_S reaches a reasonably high level, the SCP saturates and the EOP drops to deficient levels, indicating that the system's performance improvement becomes limited. Furthermore, Figure 3 investigates the impact of the Nakagami-*m* severity factor, i.e., m_1 and m_2. The SCP associated with $m_1 = 1$ and $m_2 = 1$ is the smallest, and the EOP is the largest; because, in this case, the transmission channels follow Rayleigh fading. Moreover, we observe that a higher severity factor m corresponds to a better system because the channel quality improves.

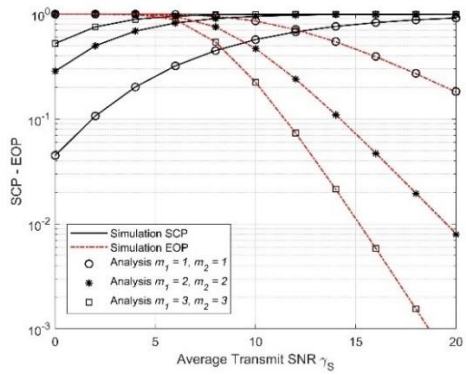

Figure 3. *SCP and EOP versus the average transmit SNR with different values of Nakagami-m severity factor*

Figure 4 clarifies the impact of two parameters, the UAV's altitude (h_U) and the energy conversion efficiency (η), on the system performance. The findings indicate the presence of an optimal flight altitude for the UAV, which yields the highest SCP and the lowest EOP.

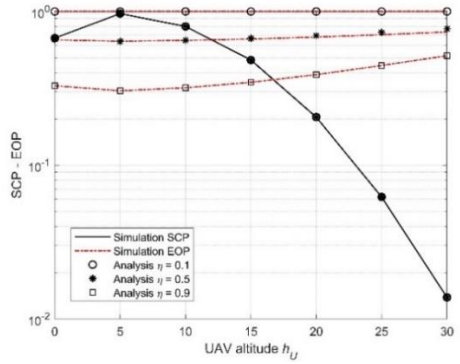

Figure 4. *SCP and EOP versus the UAV's altitude with different values of energy conversion efficiency*

This phenomenon can be attributed to the dynamic interaction between LoS and NLoS propagation as the UAV's altitude varies. Therefore, the UAV's altitude balances enhanced LoS connectivity and controlled transmission losses. This trade-off culminates in determining an optimal flight altitude that maximizes SCP while minimizing EOP. In addition, the results also show that increasing h_U reduces EOP but does not affect SCP.

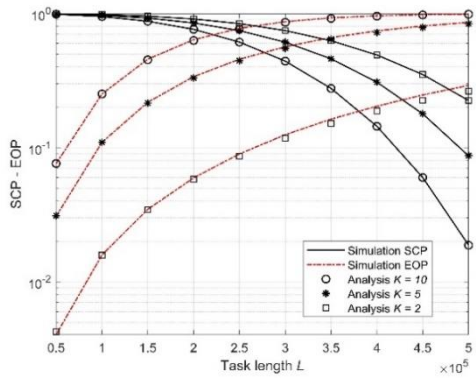

Figure 5. *SCP and EOP versus the task length with different values of number of* ***SNs***

Figure 5 depicts the impact of the task length (L) with three different number of **SN** cases: $K = 2$, $K = 5$, and

K = 10. The SCP and EOP curves both agree to show that increasing the task length will reduce the system performance. The noticeable reason is that increasing L means that the offloading and computation processes require more time and energy. Another observation is that increasing K will reduce the system performance. The reason is that the number of SN increases, requiring the MEC server at **U** to support more computations.

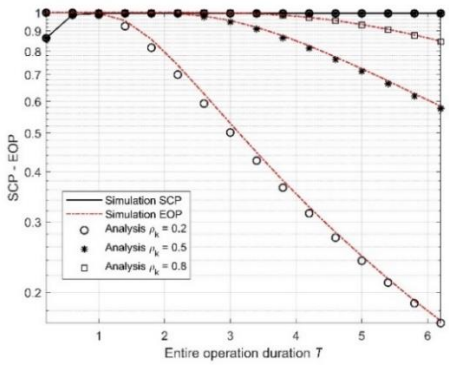

Figure 6. *SCP and EOP versus threshold of SN latency with different data dividing ratio*

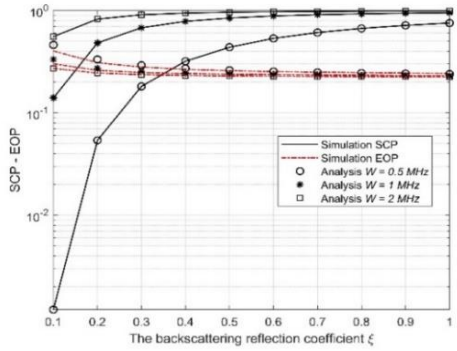

Figure 7. *SCP and EOP versus the backscattering reflection coefficient with different bandwidth level*

Figure 6 depicts system performance with data division ratio (ρ_k) and the threshold of **SN** latency (T). In the three cases, we assume that **SN**s all have the same task division coefficient, 0.2, 0.5, and 0.8, respectively. The results clearly show the significant impact of T on SCP and EOP. Specifically, when T is small, resulting in a small time slot (δ), the system performance is low, meaning low SCP and high EOP. When T is large, the time budget for the system to operate is significant, leading to increased SCP and decreased EOP. Meanwhile, ρ_k significantly impacts EOP but does not affect SCP.

In the final simulation, we investigate the system performance under the influence of the backscattering reflection coefficient (ξ) and bandwidth (W), as shown in Figure 7. As ξ increases, the smart sensor node's ability to utilize transmitter RF signals to participate in communication, thus improving system performance. Figure 7 also shows that the system performance improves as W increases.

6. Conclusion

In this paper, we investigated a backscatter-based multiple sensor node UAV-enabled MEC IoT network. We proposed the TDMA scheme, incorporating a partial offloading strategy, a backscattering framework, and an RF energy harvesting mechanism. Accordingly, we derive the approximate closed-form expressions for the SCP and EOP and use these two metrics to evaluate system performance. We investigated the impact of critical parameters such as transmit power, backscattering reflection coefficient, number of sensor nodes, task division ratio, UAV altitude, energy conversion efficiency, and threshold tolerance. The analysis is further validated through Monte-Carlo simulations. The findings of this study highlight the importance of selecting an optimal UAV altitude to improve latency and energy consumption performance. These advancements contribute to the overall goal of enabling low latency and effective energy consumption, paving the way for more reliable and sustainable 6G wireless communication systems.

Acknowledgement: This research is funded by Vietnam National Foundation for Science and Technology Development (NAFOSTED) under grant number 102.04-2021.11.

REFERENCES

[1] T Y. Mao, C. You, J. Zhang, K. Huang, and K. B. Letaief, "A survey on mobile edge computing: The communication perspective", *IEEE Commun. Surv. Tut,* vol. 19, no. 4, pp. 2322–2358, 2017.

[2] C.-X. Wang *et al.*, "On the road to 6G: Visions, requirements, key technologies, and testbeds", *IEEE Commun. Surv. Tut.*, vol. 25, no. 2, pp. 905–974, 2023.

[3] L. Shi, Y. Ye, X. Chu, S. Sun, and G. Lu, "Energy-efficient resource allocation for backscatter-assisted wireless powered mec", *IEEE Trans. Veh. Technol.*, vol. 72, no. 7, pp. 9591-9596, 2023.

[4] Q. Liu, S. Sun, X. Yuan, and Y. Zhang, "Ambient backscatter communication-based smart 5G IoT network", *EURASIP J. Wireless Commun. Netw.*, vol. 2021, no. 1, pp. 1–19, 2021.

[5] W. Wu, X. Wang, A. Hawbani, L. Yuan, and W. Gong, "A survey on ambient backscatter communications: Principles, systems, applications, and challenges", *Comput. Netw.*, vol. 216, 2022.

[6] A. Dogra, R. K. Jha, and S. Jain, "A survey on beyond 5G network with the advent of 6G: Architecture and emerging technologies", *IEEE Access*, vol. 9, pp. 67512–67547, 2021.

[7] J. Liu *et al.*, "Outage probability analysis for uav-aided mobile edge computing networks", *EAI Endorsed Trans. Ind. Netw. Intell. Sys.*, vol. 9, no. 31, e4, 2022.

[8] A. Masaracchia *et al.*, "UAV-enabled ultra-reliable lowlatency communications for 6G: A comprehensive survey", *IEEE Access*, vol. 9, pp. 137338–137352, 2021.

[9] S. H. H. Raza, D. Zorbas, and B. O'Flynn, "A comprehensive survey on RF energy harvesting: Applications and performance determinants", *Sensors*, vol. 22, no. 8, pp. 2990, 2022.

[10] S. Gong, Y. Xie, J. Xu, D. Niyato, and Y. C. Liang, "Deep reinforcement learning for backscatter-aided data offloading in mobile edge computing", *IEEE Net.*, vol. 34, no. 5, pp. 106–113, 2020.

[11] M. Abrar, U. Ajmal, Z. M. Almohaimeed, X. Gui, R. Akram, and R. Masroor, "Energy efficient UAV-enabled mobile edge computing for IoT devices: A review", *IEEE Access*, vol. 9, pp. 127779–127798, 2021.

[12] L. Shi, Y. Ye, X. Chu, and G. Lu, "Computation bits maximization in a backscatter assisted wirelessly powered mec network", *IEEE Commun. Lett.*, vol. 25, no. 2, pp. 528–532, 2021.

[13] C. Zheng and W. Zhou, "Computation bits maximization in backscatterassisted wireless-powered NOMA-MEC networks", *EURASIP J. Wireless Commun. Netw.*, vol. 23, no.1, 2022.

[14] S. Zargari, C. Tellambura, and S. Herath, "Energy-efficient hybrid offloading for backscatter-assisted wirelessly powered MEC with reconfigurable intelligent surfaces", *IEEE Trans. Mobile Comput.*, vol. 22, no. 9, pp. 5262–5279, 2023.

[15] L. Bin and Y. Rongrong, "Computing task offloading and resource allocation in UAV-enabled backscatter communications", *J. Electro. Inf. Technol.*, vol. 45, no. 7, pp. 2334–2341, 2023.

[16] B. Li, W. Liu, W. Xie, and X. Li, "Energy-efficient task offloading and trajectory planning in UAV-enabled mobile edge computing networks", *Comput. Netw.*, vol. 234, 2023.

[17] T. Hoang, Q. N. Van, L. Dung, B. Nguyen, N. Van Vinh, and T. Kim, "Performance analysis and optimization of multi-antenna UAV-aided multi-user backscatter SPC systems", *IEEE Trans. Intell. Veh.*, vol. 9, pp. 1028–1039, 2024.

[18] P. T. Tran, L. T. T. Huyen, B. C. Nguyen, H. M. Nguyen, and T. M. Hoang, "UAV-assisted finite block-length backscatter: Performance analysis and optimization", *Ad Hoc Networks*, vol. 153, pp.103352, 2024.

[19] H. A. Mohammad, Z. S. A. Raza, M. D. C., D. R. Marco, and G. Mounir, "Performance analysis of UAV enabled disaster recovery networks: A stochastic geometric framework based on cluster processes", *IEEE Access*, vol. 6, pp. 26215–26230, 2018.

[20] V. S. Nguyen and T. H. Nguyen, "Energy outage analysis of aerial UAVenabled SWIPT deployments", *IEEE Access*, vol. 12, pp. 27147–27157, 2024.

[21] A.-N. Nguyen, D.-B. Ha, V.-T. Truong, D.-T. Do, and C. So-In, "Secrecy performance analysis and optimization for UAV-relay-enabled WPT and cooperative NOMA MEC in IoT networks", *IEEE Access*, vol. 11, pp. 127800–127816, 2022.

[22] S. Liu, Y. Huang, H. Hu, J. Si, G. Cheng, T. Huang, and X. Hu, "Resource and trajectory optimization for secure communication in RIS assisted UAV-MEC system", *IET Commun.*, vol. 17, no. 18, pp. 2041–2139, 2023.

[23] Y. Ye, G. Lu, R. Q. Hu, and L. Shi, "On the performance and optimization for mec networks using uplink noma", in *IEEE Int. Conf. Commun. Works. (ICC Workshops)*, Shanghai, China, IEEE, 2019.

[24] I. Gradshteyn and I. Ryzhik, *Table of Integrals, Series, and Products*. Elsevier Academic Press, 2007.

APPENDIX A: PROOF OF THEOREM 1

For further calculation, first we derive the expressions of CDF of γ_k. By the help of (2), (3) and formula 3.471.9 [24], from the expression of γ_k as (5), after some manipulations we can obtain:

$$F_{\gamma_k}(x)=1-2\sum_{l_1=0}^{m_1-1}\frac{1}{l_1!(m_2-1)!}\upsilon^{m_2+l_1}\mathcal{K}_{m_2-l_1}(2\upsilon), \tag{A-1}$$

where $\upsilon=\sqrt{\frac{m_1m_2x}{\lambda_1\lambda_2\mu}}$, $\mathcal{K}_\nu(.)$ is the modified Bessel function of the second kind with ν^{th} order.

Deploying from the definition formula (14), we have:

$$\begin{aligned}\mathcal{P}&=\prod_{k=1}^{K}\Pr\left(t_k^{\text{off}}+t_k^c<T_k^{th},t_k^{\text{off}}+t_k^U<T_k^{th},E_k^h>0\right)\\&=\prod_{k=1}^{K}\Pr\left(t_k^{\text{off}}<T_k^{th}-t_k^c,t_k^{\text{off}}<T_k^{th}-t_k^U,t_k^{\text{off}}<\delta-t_k^c\right)\\&=\prod_{k=1}^{K}\Pr\left(\gamma_k<\max\left(\underbrace{2^{\frac{L_{k2}}{W\left(T_k^{th}-t_k^c\right)}}}_{\Lambda_1},\underbrace{2^{\frac{L_{k2}}{W\left(T_k^{th}-t_k^U\right)}}}_{\Lambda_2},\underbrace{2^{\frac{L_{k2}}{W\left(\delta-t_k^c\right)}}}_{\Lambda_3}\right)\right)\\&=\prod_{k=1}^{K}\left(1-F_{\gamma_k}\left(\max\left(\Lambda_1,\Lambda_2,\Lambda_3\right)\right)\right).\end{aligned} \tag{A-2}$$

Substituting (A-1) into (A-2), we obtain the expression of SCP as (15). This concludes our proof.

APPENDIX B: PROOF OF THEOREM 2

From the definition formula (17), we can smoothly prove that $\mathcal{E}=0$ when $E_U^c\geq E_k^{th}$ or $t_k^c\geq\delta$. The remaining cases are implemented as follows:

$$\begin{aligned}\mathcal{E}&=1-\prod_{k=1}^{K}\Pr\left(t_k^{\text{off}}<\delta-t_k^c-\frac{\Omega_1}{g_{Sk}},t_k^{\text{off}}<\Omega_2,g_{Sk}>\frac{\Omega_1}{\delta-t_k^c}\right)\\&=1-\prod_{k=1}^{K}\left[\underbrace{\Pr\left(t_k^{\text{off}}<\delta-t_k^c-\frac{\Omega_1}{g_{Sk}},\delta-t_k^c-\frac{\Omega_1}{g_{Sk}}<\Omega_2,g_{Sk}>\frac{\Omega_1}{\delta-t_k^c}\right)}_{I_1}\right.\\&\left.+\underbrace{\Pr\left(t_k^{\text{off}}<\Omega_2,\Omega_2<\delta-t_k^c-\frac{\Omega_1}{g_{Sk}},g_{Sk}>\frac{\Omega_1}{\delta-t_k^c}\right)}_{I_2}\right].\end{aligned} \tag{B-1}$$

Next, we calculate the I_1 in the case $\delta-t_k^c-\Omega_2<0$:

$$\begin{aligned}I_1&=\Pr\left(\frac{L_{k2}}{W\log_2\left(1+\mu g_{Sk}g_{Uk}\right)}<\delta-t_k^c-\frac{\Omega_1}{g_{Sk}},g_{Sk}>\underbrace{\frac{\Omega_1}{\delta-t_k^c}}_{\phi_1}\right)\\&=\int_{\phi_1}^{\infty}\left\{1-F_{g_{Uk}}\left[\frac{2^{\frac{L_{k2}}{W\left(\delta-t_k^c-\frac{\Omega_1}{x}\right)}}-1}{\mu x}\right]\right\}f_{g_{Sk}}(x)dx\\&\overset{(a)}{=}\frac{1}{(m_1-1)!}\left(\frac{m_1}{\lambda_1}\right)^{m_1}\sum_{l=0}^{m_2-1}\frac{1}{l!}\left(\frac{m_2}{\lambda_2\mu}\right)^{l}\\&\times\int_{\phi_1}^{\infty}x^{m_1-l-1}\Delta^l(x)\exp\left(-\frac{m_1}{\lambda_1}x-\frac{m_2}{\lambda_2}.\frac{\Delta(x)}{\mu x}\right)dx\\&\overset{(b)}{=}\frac{1}{(m_1-1)!}\left(\frac{m_1}{\lambda_1}\right)^{m_1}\sum_{l=0}^{m_2-1}\frac{1}{l!}\left(\frac{m_2}{\lambda_2\mu}\right)^{l}\frac{\pi\exp(-\phi_1)}{2Q}\\&\times\sum_{q=1}^{Q}\left(-\ln\left(t_q\right)\right)^{m_1-l-1}\Delta^l\left(-\ln\left(t_q\right)\right)t_q^{\frac{m_1}{\lambda_1}-1}\\&\times\exp\left(\frac{m_2}{\lambda_2}.\frac{\Delta\left(-\ln\left(t_q\right)\right)}{\mu\ln\left(t_q\right)}\right)\sqrt{1-x_q^2}.\end{aligned} \tag{B-2}$$

where step (a) is obtained by applying (2) and (3), step (b) is held by applying the Gaussian-Chebyshev quadrature method with Q is the complexity-vs-accuracy trade-off coefficient, $x_q=\cos\left(\frac{2q-1}{2Q}\pi\right)$, $t_q=\frac{x_q+1}{2}\exp(-\phi_1)$.

In the case $\delta-t_k^c-\Omega_2>0$, I_1 is rewritten as follows:

$$\begin{aligned}I_1&=\Pr\left(g_{Uk}>\frac{\Delta(x)}{\mu x},g_{Sk}<\underbrace{\frac{\Omega_1}{\delta-t_k^c-\Omega_2}}_{\phi_2},g_{Sk}>\underbrace{\frac{\Omega_1}{\delta-t_k^c}}_{\phi_1}\right)\\&\overset{(c)}{=}\frac{1}{(m_1-1)!}\left(\frac{m_1}{\lambda_1}\right)^{m_1}\sum_{l=0}^{m_2-1}\frac{1}{l!}\left(\frac{m_2}{\lambda_2\mu}\right)^{l}\frac{\pi(\phi_2-\phi_1)}{2Q}\\&\times\sum_{q=1}^{Q}l_q^{m_1-l-1}\Delta^l\left(l_q\right)\exp\left(-\frac{m_1}{\lambda_1}l_q-\frac{m_2}{\lambda_2}.\frac{\Delta\left(l_q\right)}{\mu l_q}\right)\sqrt{1-l_q^2}.\end{aligned} \tag{B-3}$$

where step (c) is held by applying the Gaussian-Chebyshev quadrature method with $l_q=\frac{x_q+1}{2}(\phi_2-\phi_1)$. Using precisely the same method, we can calculate I_2. This ends our proof.